

PAPER

Electron–phonon superconductivity in C-doped topological nodal-line semimetal Zr_5Pt_3 : a muon spin rotation and relaxation (μSR) study







To cite this article: A Bhattacharyya *et al* 2022 *J. Phys.: Condens. Matter* **34** 035602

View the [article online](#) for updates and enhancements.

You may also like

- [Chiral p-wave order in \$\text{Sr}_2\text{RuO}_4\$](#)
Catherine Kallin
- [SR investigation of the intercalated graphite superconductor \$\text{CaC}_6\$](#)
T Shiroka, G Lamura, R De Renzi *et al.*
- [SR study of \$\text{CeRhIn}_5\$ under applied pressure](#)
R H Heffner, T Goko, D Andreica *et al.*

Electron–phonon superconductivity in C-doped topological nodal-line semimetal Zr_5Pt_3 : a muon spin rotation and relaxation (μSR) study

A Bhattacharyya^{1,*} , P P Ferreira^{2,*} , K Panda¹ , S H Masunaga^{3,4},
L R de Faria² , L E Correa², F B Santos², D T Adroja^{5,6} , K Yokoyama⁵ ,
T T Dorini⁷, R F Jardim⁴, L T F Eleno² and A J S Machado²

¹ Department of Physics, Ramakrishna Mission Vivekananda Educational and Research Institute, Howrah 711202, India, Howrah 711202, West Bengal, India

² Escola de Engenharia de Lorena, Universidade de São Paulo, DEMAR, Lorena, Brazil

³ Departamento de Física, Centro Universitário FEI, São Bernardo do Campo, Brazil

⁴ Instituto de Física, Universidade de São Paulo, Rua do Matão, 1371, 05508-090, São Paulo, SP, Brazil

⁵ ISIS Facility, Rutherford Appleton Laboratory, Chilton, Didcot, Oxon, OX11 0QX, United Kingdom

⁶ Highly Correlated Matter Research Group, Physics Department, University of Johannesburg, Auckland Park 2006, South Africa

⁷ Université de Lorraine, CNRS, IJL, Nancy, France

E-mail: amitava.bhattacharyya@rkmvu.ac.in and pedroferreira@usp.br

Received 20 April 2021, revised 28 September 2021

Accepted for publication 30 September 2021

Published 2 November 2021



Abstract

In the present work, we demonstrate that C-doped Zr_5Pt_3 is an electron–phonon superconductor (with critical temperature $T_C = 3.8$ K) with a nonsymmorphic topological Dirac nodal-line semimetal state, which we report here for the first time. The superconducting properties of $\text{Zr}_5\text{Pt}_3\text{C}_{0.5}$ have been investigated by means of magnetization, resistivity, specific heat, and muon spin rotation and relaxation (μSR) measurements. We find that at low temperatures, the depolarization rate is almost constant and it can be well described by a single-band *s*-wave model with a superconducting gap of $2\Delta(0)/k_B T_C = 3.84$, somewhat higher than the value of BCS theory. From the transverse field μSR analysis, we estimate the London penetration depth $\lambda_L = 469$ nm, superconducting carrier density $n_s = 1.83 \times 10^{26} \text{ m}^{-3}$, and effective mass $m^* = 1.428m_e$. The zero field μSR confirms the absence of any spontaneous magnetic field in the superconducting ground state. In order to gain additional insights into the electronic ground state of C-doped Zr_5Pt_3 , we also performed first-principles calculations within the framework of density functional theory (DFT). The observed homogenous electronic character of the Fermi surface as well as the mutual decrease of T_C and density of states at the Fermi level are consistent with the experimental findings of this study. However, the band structure reveals the presence of robust, gapless fourfold-degenerate nodal lines protected by 6_3 screw rotations and glide mirror planes. Therefore, Zr_5Pt_3 represents a novel, unprecedented condensed matter system to investigate the intricate interplay between superconductivity and topology.

Keywords: superconductivity, muon spin rotation and relaxation

* Authors to whom any correspondence should be addressed.

(Some figures may appear in colour only in the online journal)

1. Introduction

The search for new superconductors is a cornerstone in quantum matter physics. In particular, the study of how the superconducting state evolves with doping and pressure has been essential to understand the fundamental mechanisms of Cooper pairs condensation and their competition among different coherent states. However, in the last few years we are seeing a new chapter being written, where the topological nature of matter is responsible for the emergence of a wide range of novel quantum states. Topological insulators and symmetry-protected topological semimetals can exhibit quantized anomalous Hall effect [1–3], ultrahigh electronic mobility [4–6], giant magnetoresistance [7, 8], chiral anomaly [9–12], and gapless, robust edge states [13–15], to cite a few examples. When combined with superconductors, topological materials could also harbor Majorana quasiparticles with non-Abelian exchange statistics, thus possibly opening the way for the quantum computation era [16].

In this context, a large number of intermetallic compounds with general formula M_5X_3 (M is either a transition or rare earth metal and X is a metalloid) represent a novel platform to explore a plethora of unique properties [17–26]. These compounds can crystallize in three different prototypes: (i) orthorhombic Yb_5Sb_3 ($Pnma$, No. 62), (ii) tetragonal Cr_5B_3 ($I4/mcm$, No. 140), and (iii) hexagonal Mn_5Si_3 ($P6_3/mcm$, No. 193). Among them, the Mn_5Si_3 structure can interstitially host a third element (carbon, boron, nitrogen or oxygen) at $2b$ Wyckoff position. Physical properties of more than 500 compounds in this hexagonal structure have been reported so far. Superconductivity is observed only in few compounds though, such as Zr_5Sb_3 ($T_C = 2.3$ K) [18], Zr_5Pt_3 ($T_C = 6.4$ K) [24], tetragonal ($T_C = 2.8$ K) and hexagonal ($T_C = 9.4$ K) Nb_5Ir_3 [22], and Nb_5Ge_3 ($T_C = 0.3$ K) [26]. In Nb_5Ir_3 , for instance, T_C increases to 10.5 K with oxygen doping [20] and a crossover from multiple to single gap superconductivity with increasing Pt content was reported in $Nb_5Ir_{3-x}Pt_xO$ [19]. On the other hand, the addition of oxygen in Zr_5Pt_3 reduces monotonically the critical temperature from 6.4 K to 3.2 K ($Zr_5Pt_3O_{0.6}$) [24]. Likewise, T_C of Zr_5Sb_3 decreases with the addition of oxygen until the suppression of the superconducting phase in Zr_5Sb_3O [18]. The highest reported T_C in this family, however, belongs to $Nb_5Ge_3C_{0.3}$ [23], with $T_C = 15.3$ K.

Recently, Renosto *et al* reported a comprehensive study of the effects of carbon doping on the superconducting properties of $Zr_5Pt_3C_x$ [25]. It was found that T_C first increases from 6 K ($x = 0$) to 7 K ($x = 0.3$) and further decreases monotonously for $x > 0.3$ [25]. However, by measuring the lower and upper critical fields and the temperature dependence of penetration length and specific heat, the authors argued that $Zr_5Pt_3C_{0.3}$ strongly deviates from the conventional

s -wave pairing behavior, suggesting thus an unconventional superconductivity driven by carbon doping.

Motivated by these results, we show, using muon spin relaxation and rotation (μ SR) measurements combined with first-principles electronic-structure calculations, that a conventional, single-gap s -wave superconducting order parameter within the weak-coupling limit is sufficient to describe the superconducting ground state of $Zr_5Pt_3C_{0.5}$. As far as we know, this is the first systematic μ SR study on the superconducting properties of doped M_5X_3 -type compounds. Furthermore, we demonstrate that Zr_5Pt_3 is a topological nodal-line semimetal protected by nonsymmorphic symmetries. In contrast to Dirac/Weyl semimetals, where the conduction and valence bands touch at discrete points in the Brillouin zone and disperse linearly in all momentum directions [27], in nodal-line semimetals the linear band-crossing points form closed loops in momentum space, opening the way to novel quantum phases, such as nearly flat drumhead-like surface states [28–30]. In this vein, Zr_5Pt_3 -type compounds represent an unprecedented, large family of superconducting nodal-line semimetals, still to be explored in more details.

2. Experimental details

2.1. Sample preparation and physical properties measurements

The sample was prepared using high-purity (99.99%) pieces of Zr, Pt and C in the $Zr_5Pt_3C_{0.5}$ stoichiometry. The pieces were arc-melted together several times in a water-cooled copper hearth under a Ti-gettered ultra high-pure argon atmosphere. The resulting ingot was sealed under vacuum in a quartz ampoule and annealed at 1100 °C for 7 days. X-ray powder diffraction (XRD) scans were taken with a panalytical Empyrean diffractometer with $Mo-K_\alpha$ radiation, and analyzed using the HighScore plus software based on the Rietveld method for structural refinement. A part of the sample was mounted and polished for a scanning electron microscope (SEM) analysis that was performed in a Hitachi TM-3000 SEM equipped with an Oxford energy dispersive spectrometer (EDS).

A thin slab of the sample was prepared for magnetization, electrical resistivity and heat capacity measurements using a DynaCool physical properties measurement system (PPMS). Zero-field-cooled (ZFC) and field-cooled (FC) magnetization as a function of temperature were obtained under magnetic field of 30 Oe. Isothermal magnetization data as a function of the applied magnetic field data were collected using a vibrating sample magnetometer. Resistivity data was measured using the standard four-probe method between 1.8 K and 300 K. The temperature dependence of the lower critical field (H_{C1}) was extracted from the magnetization curves below T_C and

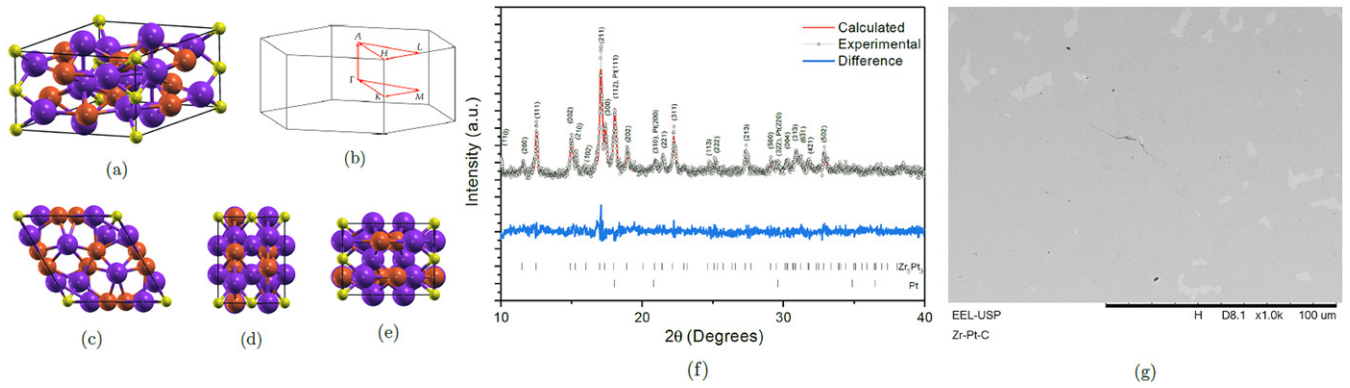


Figure 1. (a) Hexagonal Zr_5Pt_3C unit cell with space group $P6_3/mcm$ (no. 193). Purple, orange, and yellow spheres represent Zr, Pt, and C, respectively. (b) First Brillouin zone of Zr_5Pt_3 system with the path along high-symmetry points. The a - b , a - c , and c - b planes are shown in (c), (d) and (e), respectively. (f) XRD data. The symbols represent the experimental data and the lines are the Rietveld refinement. (g) SEM micrograph ($1000\times$) of $Zr_5Pt_3C_{0.5}$. The continuous dark gray region corresponds to the $Zr_5Pt_3C_{0.5}$ main phase along with a small amount of isolated light gray Pt grains.

the temperature dependence of the upper critical field (H_{C2}) was obtained from the midpoint of the resistivity transitions for several applied fields. Heat capacity measurements were carried out using the calorimeter option of the PPMS, which uses a relaxation method.

2.2. μ SR measurements

μ SR measurements were carried out at the ISIS Neutron and Muon Source of STFC Rutherford Appleton Laboratory, UK, on the MUSR spectrometer. 64 detectors are placed in transverse and longitudinal directions to detect the asymmetry of the positrons [31]. In the sample, 100% spin-polarized positive muons are implanted, which decay with a half-life of $2.2 \mu s$, decaying into a positron and a pair of neutrinos. As the positrons are preferentially emitted along the muon spin vectors, information on the local magnetic field distribution at the muon stopping site can be obtained by detecting the asymmetry of the emitted positrons. The time-dependent symmetry $A(t)$ of the μ SR spectra is given by $A(t) = \frac{N_F(t) - \alpha N_B(t)}{N_F(t) + \alpha N_B(t)}$, where $N_F(t)$ and $N_B(t)$ are the number of positrons counted in the forward and backward detectors, respectively, and α is an instrumental calibration factor. Zero-field μ SR (ZF) is carried out in the longitudinal set up of the detectors. A correction coil is applied to neutralize any stray magnetic fields up to 10^{-3} G. The transverse field (TF) measurements were carried with detectors in a transverse arrangement, with a field of 300 G (well below the upper critical field $H_{C2} = 6.3 \times 10^4$ G) applied perpendicular to the initial muon polarization direction [32].

The $Zr_5Pt_3C_{0.5}$ sample was powdered and placed in a high purity (99.995%) silver sample holder using diluted GE-varnish and then wrapped with thin silver foil, since the signal from muons stopping in silver depolarizes at a negligible rate. All data analysis were done using WiMDA [33] software.

2.3. Computational methods

First-principles electronic-structure calculations were performed within the Kohn–Sham scheme [34] of the density functional theory (DFT) [35] with full-relativistic projec-

tor augmented plane wave pseudopotentials [36] as implemented in quantum Espresso [37, 38]. Exchange and correlation effects were treated with the local density approximation as described by the Perdew–Zunger (PZ) parametrization [39]. We have used a wave function energy cut-off of 80 Ry ($1 \text{ Ry} \approx 13.6 \text{ eV}$), and 800 Ry for the charge density and potential kinetic energy cut-off. The Monkhorst–Pack scheme [40] was used for a $8 \times 8 \times 12$ k -point sampling in the first Brillouin zone. A denser $16 \times 16 \times 24$ k -point sampling was further used to obtain the band structure, density of states (DOS) and Fermi surface. Self-consistent-field calculations were carried out using a Marzari–Vanderbilt smearing [41] of 0.005 Ry. All lattice parameters and internal degrees of freedom were relaxed in order to guarantee a ground-state convergence of 10^{-5} Ry in total energy and $0.5 \text{ mRy}/a_0$ ($a_0 \approx 0.529 \text{ \AA}$) for forces acting on the nuclei.

3. Results and discussion

3.1. Crystal structure and physical characterization

Zr_5Pt_3 crystallizes in a hexagonal Mn_5Si_3 -type structure ($P6_3/mcm$, No. 193), as displayed in figure 1(a). The XRD scans from figure 1(f) show the presence of the $Zr_5Pt_3C_{0.5}$ phase, with a small amount of additional Pt, which represents 1.7% of the weight fraction of the crystalline phases. The Rietveld analysis resulted in lattice parameters of $a = 8.153 \text{ \AA}$ and $c = 5.457 \text{ \AA}$, which indicates a contraction (expansion) of the in-plane (out-of-plane) axis, probably due to the presence of carbon, as will be discussed in section 4. No mass loss has been detected in the synthesis which confirms the amount of carbon is 0.5 in sample. The EDS analysis on the SEM shows a 1.73 ratio of Zr/Pt instead of the expected 1.67 for Zr_5Pt_3 , which is consistent with the observation of free Pt in both XRD and SEM. Nevertheless, as can be seen in figure 1(g), the 1.7% excess Pt is the weight fraction of the Pt phase that appears in isolated pockets in a continuous Zr_5Pt_3 matrix that allows a good characterization of the physical properties of the main phases.

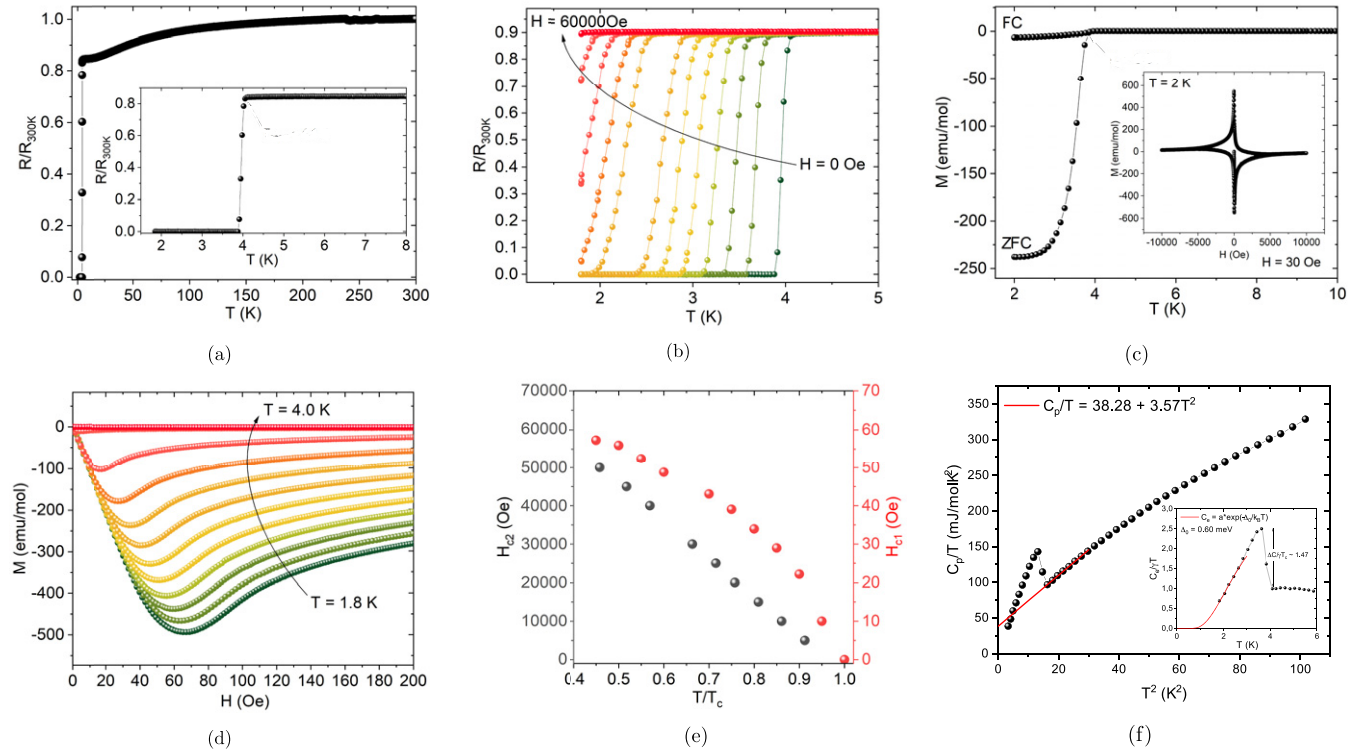


Figure 2. (a) Electrical resistance versus temperature. The inset shows the low temperature dependence of the electrical resistance. (b) Resistance as a function of temperature under different applied magnetic fields. (c) Temperature variation of the dc magnetic susceptibility in the presence of an applied field of 30 Oe, collected in the FC and the ZFC modes. The inset shows the field dependence of the isothermal magnetization at 2 K. (d) Magnetization dependence with the applied magnetic field within the 1.8–4.0 K temperature range. (e) Upper (black) and lower (red) critical fields as a function of reduced temperature. (f) Temperature dependence of the specific heat for $Zr_5Pt_3C_{0.5}$. The inset depicts the BCS-type anomaly.

Figure 2(a) shows the sample’s resistance versus temperature data is shown in figure 2(a), where the zero-resistance state is clearly observed at 3.8 K. The downward curvature of the normal state is consistent with the presence of an extra phase and a certain level of disorder. The values for resistance as function of temperature under several applied magnetic fields are shown in figure 2(b). They were used to determine the temperature dependence of H_{C2} taking into account the midpoint of the transition. A strong diamagnetic behavior indicating the onset of the superconductivity near $T_C = 3.8$ K is observed in the ZFC magnetization versus temperature data, as shown in figure 2(c), which is an indicative of bulk superconductivity in $Zr_5Pt_3C_{0.5}$. The rectangular cuboid geometry of the sample with $2.5 \times 1.5 \times 0.3$ mm yields a demagnetization factor of 0.8065 [42], which, in turn, results in a superconducting volume fraction of 92%. The insert contains the magnetization versus the applied magnetic field, showing a well-developed hysteresis loop for the Meissner state.

A complete set of isothermal M vs H curves in the temperature range of 1.8 K to 4.0 K is shown in figure 2(d). The H_{C1} vs T dependence was obtained by taking the value at which the experimental data deviates by $dM = 10^{-3}$ emu from the linear behavior. We have estimated the coherence length ξ_{GL} as 7.81 nm using the relation $H_{C2}(0) = \frac{\phi_0}{2\pi\xi_{GL}^2}$ and $H_{C2}(0) = 5.4$ T, where ϕ_0 ($=2.07 \times 10^{15}$ T m²) is the magnetic flux quantum. The Ginzburg–Landau(GL) parameters

$\kappa_{GL} = \frac{\lambda(0)}{\xi_{GL}(0)} = 60$, where λ ($=469$ nm) is the magnetic penetration depth, shows that the alloy is a type-II superconductor. A plot of H_{C1} vs T/T_C in figure 2(e) reveals a deviation from the expected behavior in single-band BCS superconductors. Interestingly, the H_{C2} deviates from the expected conventional scenario as well. Such discrepancies in the critical field behavior could be explained by either considering a multiband scenario, in which electrons on two different bands contribute to superconductivity, or by an anisotropic band giving rise to superconductivity. In the first case, it would be expected that the opening of two superconducting gaps at the Fermi surface would affect the heat capacity anomaly. However, figure 2(f) shows a well-developed peak in the C_P/T vs T^2 data. The electronic contribution to the heat capacity is shown in the insert, with a jump size of 1.47, consistent with the BCS value of 1.43 for single-band conventional superconductors. Therefore, based on the temperature dependence of the specific heat, a multiband scenario is unlikely. Above T_C in the normal state, the $C_P(T)$ data can be described using $C_P/T = \gamma + \beta T^2$, where γT is the electronic heat capacity coefficient and βT^3 is the lattice (phonon) contribution to the specific heat, which yields $\gamma = 38.28$ mJ mol⁻¹ K⁻² and $\beta = 3.57$ mJ mol⁻¹ K⁻⁴. Using the Debye model, the Debye temperature is given by $\Theta_D = (\frac{12\pi^4 nR}{5\beta})^{1/3}$ where $R = 8.314$ J mol⁻¹ K⁻¹ is the gas constant and n is the number of atoms per formula unit. Using this relationship, Θ_D is estimated to be 167 K. The inset of

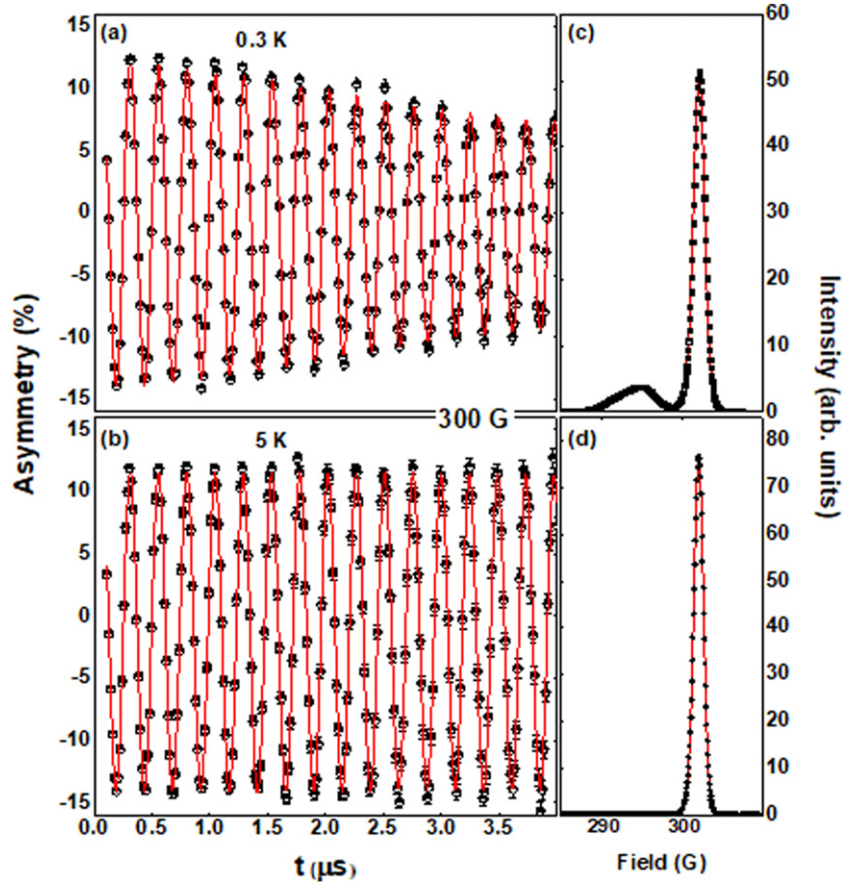


Figure 3. (a) Time dependence of TF μ SR asymmetry spectra collected at (a) $T = 0.3$ K ($<T_C$) and (b) $T = 5$ K ($>T_C$) in the presence of an applied field $H = 300$ G. The red solid line shows the fit to the data using equation (1). (c) and (d) display the corresponding maximum entropy spectra (below and above T_C).

figure 2(f) displays the temperature dependence of electronic heat capacity ($C_e(T)$) obtained by subtracting the phonon contribution from $C_p(T)$. $C_e(T)$ can be used to investigate the superconducting gap symmetry. From the fit to the exponential temperature dependence of $C_e(T)$ shown in the inset of figure 2(f). We find $\Delta(0) = 0.6$ meV, which yields $2\Delta(0)/k_B T_C = 3.85$, which, in turn, falls within the expected range from 3 to 4.5 for BCS superconductors [43].

3.2. TF- μ SR analysis

TF- μ SR measurements were performed from 0.3 K to 5 K. The observed asymmetries, at 0.3 K and 5 K, below and above T_C respectively, can be found in figures 3(a) and (b). Fourier transformation of the respective asymmetry spectra and the maximum entropies are shown in figures 3(c) and (d). It is clear that in figure 3(c) there is a sharp narrow peak around the applied field and an additional broad peak, which corresponds to the presence of a magnetic field smaller than the applied TF. This additional peak is absent in figure 3(d). In the mixed state, such distribution is a clear indicator of a type-II superconductor [44]. In the superconducting state at 0.3 K, it is clear that the spectra strongly depolarize due to the inhomogeneous distribution of the internal field derived from the formation of the vortex state. Meanwhile, at 5 K the spectra depolarization is quite negligible, which can be attributed to the nuclear

moments of the silver background. The time spectra can be fitted using an oscillatory Gaussian decay function and an oscillatory function, which arises due to the silver sample holder. [45–47],

$$G_{TF}(t) = A_{sc} \cos(\omega_{sc}t + \phi) \exp\left(-\frac{\sigma_T^2 t^2}{2}\right) + A_{bg} \cos(\omega_{bg}t + \phi), \quad (1)$$

where the initial asymmetries associated with both sample and background are represented by A_{sc} ($= 86.8\%$) and A_{bg} ($= 13.2\%$), respectively, ω_{sc} and ω_{bg} are the frequencies of the muon spin precession frequency from the sample and background, and ϕ is the phase offset. The Gaussian depolarization rate σ_T has two contribution below T_C , where σ_{sc} is derived from a superconducting component and σ_{nm} ($= 0.0852 \mu\text{s}^{-1}$) is derived from a nuclear magnetic dipolar moment that is constant over the whole temperature range, later assisted by the ZF- μ SR. Thus, the contribution from the vortex lattice, σ_{sc} , was calculated by quadratically subtracting σ_{nm} obtained from the fitting of the spectra measured above T_C . The field shift is $\Delta B = B_{SC} - B_{app}$, where B_{SC} indicates the superconducting field induced by the vortex lattice and B_{app} is the applied field, as shown in figure 4(b). As the sample goes through the transition into the superconducting state, there is a strong negative shift in the peak field, which is a

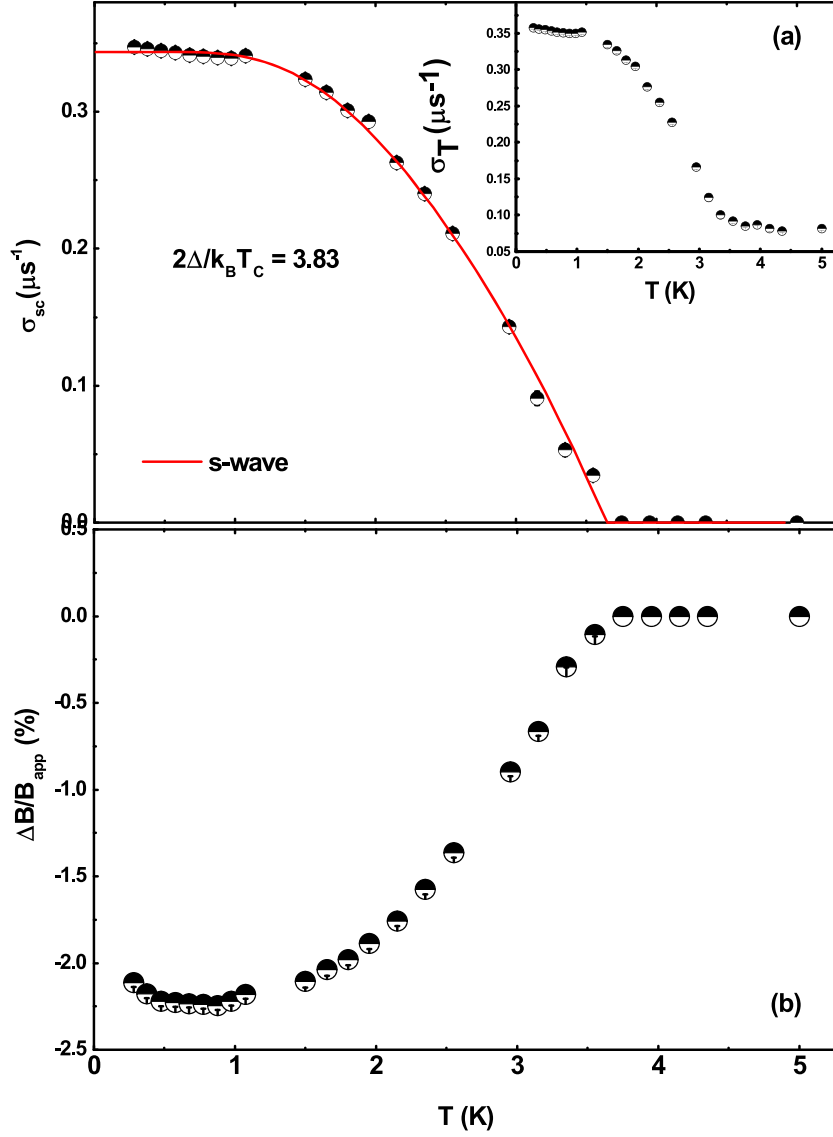


Figure 4. (a) The temperature variation of superconducting depolarization rate $\sigma_{sc}(T)$. The solid red line shows the fit using *s*-wave model. Inset shows the total muon spin depolarization rate σ_T as a function of temperature. (b) The relative change of the internal field normalized to external applied field as a function of temperature, where $\Delta B = B_{SC} - B_{app}$.

unique characteristic of the vortex lattice [48, 49]. Figure 4(a) presents $\sigma_{sc}(T)$ as a function of temperature, which is proportional to the superfluid density, thus providing details about the gap structure. It is clear that at low temperature the σ_{sc} is almost constant, which indicates a fully gapped superconducting state. The normalized superfluid density was modelled using [50–54]

$$\frac{\sigma_{sc}(T)}{\sigma_{sc}(0)} = \frac{\lambda^{-2}(T)}{\lambda^{-2}(0)} \quad (2)$$

$$= 1 + \frac{1}{\pi} \int_0^{2\pi} \int_{\Delta(T,\phi)}^{\infty} \left(\frac{\delta f}{\delta E} \right) \times \frac{E dE d\phi}{\sqrt{E^2 - \Delta(T,\phi)^2}}.$$

Here, f is the Fermi function, that can be represented by $f = [1 + \exp(E/k_B T)]^{-1}$, and $\Delta(T, \phi) = \Delta_0 \delta(T/T_C) g(\phi)$, whereas $g(\phi)$ is the angular dependence of the gap function. The azimuthal angle in the direction of the Fermi

surface is denoted by ϕ . The temperature variation of the superconducting gap is approximated by the relation $\delta(T/T_C) = \tanh\{1.82[1.018(T_C/T - 1)]^{0.51}\}$. $g(\phi)$, the spatial dependence, is substituted by 1 for *s*-wave symmetry. Using this, we find that the data is best modelled considering a single isotropic *s*-wave gap of 0.59 meV, which is consistent with 0.6 meV obtained from electronic heat capacity data, yields $2\Delta(0)/k_B T_C = 3.84$, somewhat higher than 3.53 predicted for weak-coupling BCS superconductors. Below T_C the electronic specific heat capacity (C_e) is well described by BCS gap model [25].

The depolarization rate (σ_{sc}) recorded below T_C is correlated with the superfluid density or the penetration depth. For a triangular lattice, $\frac{\sigma_{sc}^2}{\gamma_\mu^2} = \frac{0.00371 \times \phi_0^2}{\lambda^4}$ [55–57], where ϕ_0 is the flux quantum number (2.07×10^{-15} T m²) and γ_μ is the muon gyromagnetic ratio $\gamma_\mu/2\pi = 135.5$ MHz T⁻¹. Superfluid density can also be related to quantities at the atomic

Table 1. The superconducting parameters of $\text{Zr}_5\text{Pt}_3\text{C}_{0.5}$.

Parameters	$\text{Zr}_5\text{Pt}_3\text{C}_{0.5}$
T_C (K)	3.8
H_{c1} (Oe)	59
H_{c2} (kOe)	54
ξ_{GL} (nm)	7.81
κ	60.05
$\gamma(0)$ ($\text{mJ mol}^{-1}\text{K}^{-2}$)	38.28
β ($\text{mJ mol}^{-1}\text{K}^{-4}$)	3.57
Θ_D (K)	167
$\Delta C/\gamma T_C$	1.47
$2\Delta/k_B T_C$	3.84
λ (nm)	469
λ_{e-ph}	0.428
n_s (carriers m^{-3})	1.83×10^{26}

order, as with other phenomenological parameters that characterize the superconducting state. Using London's theory, [?] $\lambda_L^2 = \frac{m^* c^2}{4\pi n_s e^2}$, where $m^* = (1 + \lambda_{e-ph})m_e$ is the effective mass and n_s is the density of superconducting carriers. Within this simple picture, λ_L is independent of magnetic field. λ_{e-ph} is the electron–phonon coupling parameter that can be estimated from the Debye temperature (Θ_D) and T_C using the semi-empirical McMillan equation [58],

$$\lambda_{e-ph} = \frac{1.04 + \mu^* \ln(\Theta_D/1.45T_C)}{(1 - 0.62\mu^*) \ln(\Theta_D/1.45T_C) - 1.04}, \quad (3)$$

where μ^* is a repulsive electron–electron pseudopotential with typical values at the order of $\mu^* = 0.1$ and $\Theta_D = 167$ K, which gives $\lambda_{e-ph} = 0.428$. Being a type-II superconductor we can assume that the density of the normal state carriers is approximately equal to the density of superconducting carriers ($n_s \approx n_e$) as has been assumed in the case of ThFeAsN , $\text{K}_2\text{Cr}_3\text{As}_3$ and $\text{Cs}_2\text{Cr}_3\text{As}_3$ [45, 46, 55]. Therefore, the density of the superconducting carriers (n_s), their effective-mass (m^*), and London penetration depth (λ_L) can be estimated, respectively, as $n_s = 1.83 \times 10^{26}$ carriers m^{-3} , $m^* = 1.428m_e$, and $\lambda_L(0) = 469$ nm (table 1).

3.3. ZF- μ SR analysis

ZF- μ SR is used to investigate the existence of any spontaneous magnetic moment in the superconducting ground state [59–61]. The evolution of the ZF-asymmetry spectra over time is displayed in figure 5 for $T = 0.3$ K ($<T_C$) and $T = 5$ K ($>T_C$). The spectra below and above T_C are found to be similar, ruling out the presence of spontaneous magnetic field, which implies that time-reversal symmetry (TRS) is preserved in the superconducting state of $\text{Zr}_5\text{Pt}_3\text{C}_{0.5}$. The ZF- μ SR data was fitted using a Lorentzian function with a constant background [62]:

$$G_{ZF}(t) = A_0 \exp(-\lambda t) + A_{bg}. \quad (4)$$

Here, A_0 is the sample asymmetry and A_{bg} is the background asymmetry, which are almost independent of the temperature. The parameter λ is the rate of relaxation resulted from the nuclear moments. In figure 5, the red line indicates the

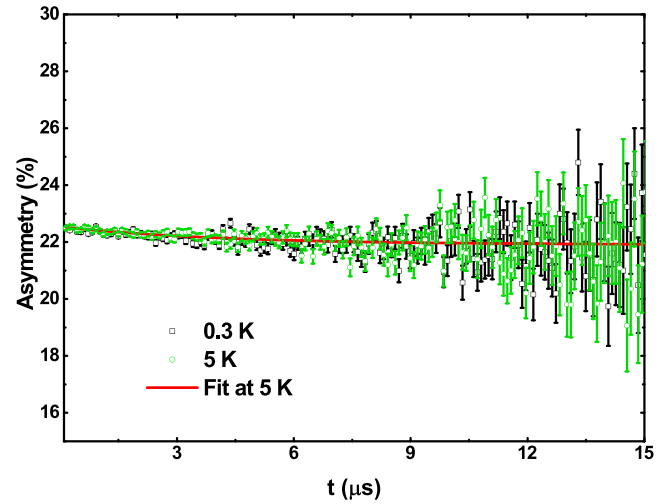


Figure 5. Time evolution of ZF- μ SR asymmetry spectra at 0.3 K (black squares) and 5 K (green circles), presented together. The red line is the least squares fit to the data using equation (4).

obtained fit for ZF- μ SR data using equation (4). The parameters obtained from the ZF- μ SR asymmetry data are as follows: $\lambda = 0.291 \mu\text{s}^{-1}$ at 0.3 K and $\lambda = 0.242 \mu\text{s}^{-1}$ at 5 K. The shift in the relaxation rate is within the error bar, indicating that TRS is preserved in $\text{Zr}_5\text{Pt}_3\text{C}_{0.5}$.

4. Theoretical calculations

The electronic band structure, partial DOS, and Fermi surface of Zr_5Pt_3 , $\text{Zr}_5\text{Pt}_3\text{C}_{0.5}$, and $\text{Zr}_5\text{Pt}_3\text{C}$ including spin–orbit coupling (SOC) effects are shown in figures 6(a)–(c), with the corresponding DOS at the Fermi level, $N(E_F)$, and optimized lattice parameters. With the increasing of C content x , the a (c) lattice parameter decreases (increases) monotonically, reflecting a stronger in-plane hybridization between C-p and Zr-d states. There are six bands crossing the Fermi energy in Zr_5Pt_3 (see figure 6(a)), which results in a high DOS at the Fermi level of 18.3 eV^{-1} , with approximately 68% of these carriers derived from the Zr-d manifold. The change in $N(E_F)$ with increasing x from 0 to 0.5 in $\text{Zr}_5\text{Pt}_3\text{C}_x$ is almost -5.5% , which can be partially associated with the quasi-rigid band tuning of the chemical potential and the respective suppression of the ϵ sheet in the Fermi surface up to $x = 1$.

Although its complex, disconnected multiband nature, the homogeneous distribution of the electronic character of the Fermi surface shows an evident contrast from the usual signature presented by the Fermi surface of multiband superconductors, which generally presents very distinct orbital characters and an anisotropic hybridization on distinct sheets, and, as consequence, the average of the electron–phonon scattering connecting different points at Fermi surface are disjointed relative to the band index [63–71]. The mutual monotonic decrease of the DOS at the Fermi level and the observed superconducting critical temperature with the carbon doping [25] is compatible with the BCS theory as well. Therefore, in the light of our theoretical and experimental findings, the single-band electron–phonon s -wave pairing within weak coupling limit may

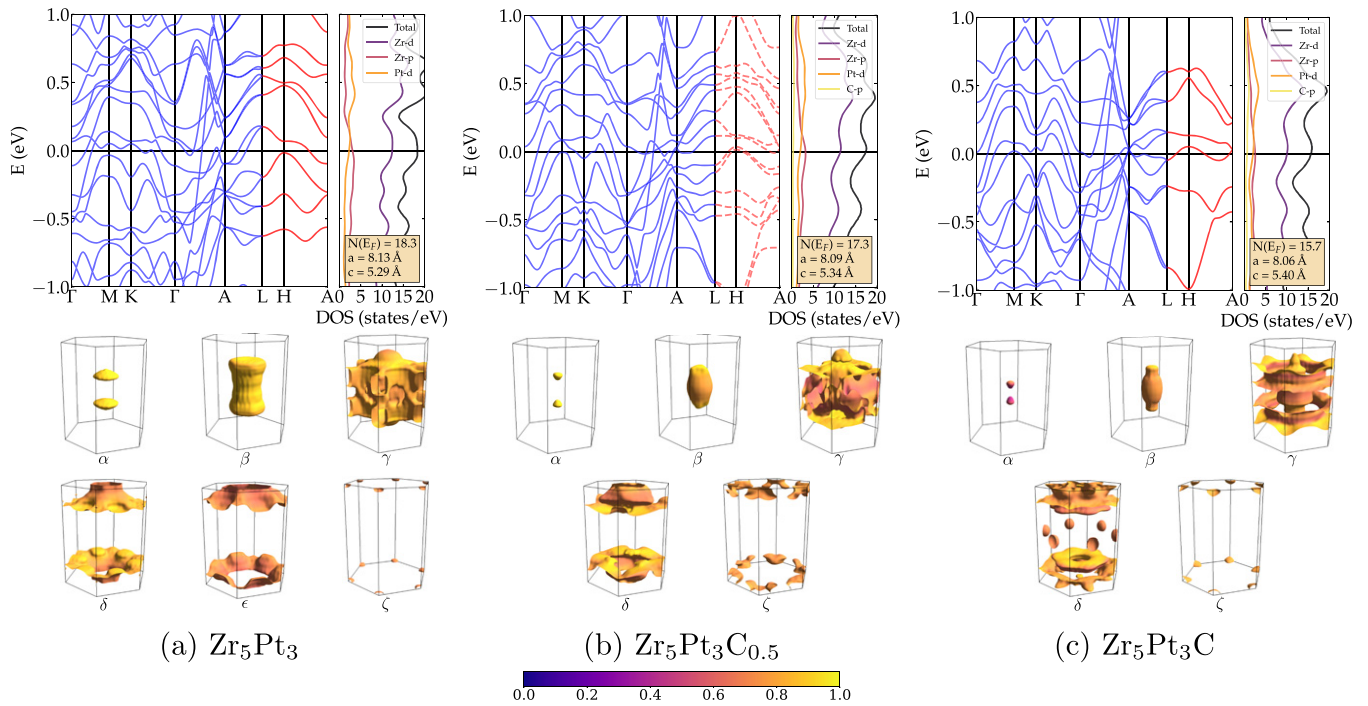


Figure 6. Electronic structure, partial DOS, and Fermi surface of (a) Zr_5Pt_3 , (b) $\text{Zr}_5\text{Pt}_3\text{C}_{0.5}$, and (c) $\text{Zr}_5\text{Pt}_3\text{C}$. Also shown are the total DOS at the Fermi level, $N(E_F)$, and the relaxed lattice parameters. The gapless nodal lines protected by the nonsymmorphic 6_3 screw rotation symmetry of space group $P6_3/mcm$ are highlighted by solid red lines in the band structure diagram. The color map in the Fermi surfaces indicates the contribution of Zr-d orbitals in the low-energy states' wave functions.

be considered a coherent mechanism for superconductivity in Zr_5Pt_3 system.

Interestingly, our calculations reveal that Zr_5Pt_3 is a nonsymmorphic topological Dirac nodal-line semimetal [72–75], as explained below. In the presence of SOC all bands are twofold-degenerate due to the presence of both time-reversal and inversion symmetries. Along Γ – A we can observe the presence of several linear band crossings in the vicinity of the Fermi level. Such fourfold-degenerate gapless Dirac nodes along Γ – A are protected against SOC by C_3 rotational symmetry of the double point group C_{6v} , since both twofold-degenerate electronic dispersions that originate the band crossings, with distinct irreducible representations, possess different rotation eigenvalues on the out-of-plane axis [76–79]. However, pairs of twofold-degenerate bands along A – L merge into single, degenerate bands along L – H – A , that is, along $k_z = \pi/c$ plane, which creates symmetry-enforced fourfold-degenerate nodal lines (solid red lines in figure 6). These nodal lines are protected by 6_3 screw rotations with centre of symmetry in the $2b$ Wyckoff position and axial glide mirror planes of the $P6_3/mcm$ space group, which means that they are robust against any perturbations as long as the nonsymmorphic symmetries hold. In fact, the presence of nonsymmorphic symmetries, such as screw rotations and glide mirror symmetries, support antrivial band connection at the Brillouin zone boundary [78].

The nonsymmorphic protection of the nodal lines are demonstrated in figure 6(b), where we show the band structure of $\text{Zr}_5\text{Pt}_3\text{C}_{0.5}$. In this structure only half of the $2b$ Wyckoff positions are filled, thus explicitly breaking the center of

symmetry of the 6_3 screw axis and the fractional translation of the glide mirror planes. Consequently, the nodal lines are gapped due to the SOC effect, as represented by the dashed red lines along L – H – A , and the Fermi surface acquire a distortive topography. However, when the nonsymmorphic symmetries are preserved, by completely filling out the $2b$ positions in $\text{Zr}_5\text{Pt}_3\text{C}$ (figure 6(c)), the nodal-line states remain protected. At this point it is important to note that, on average, effective point-group symmetries can be preserved in a homogeneously, perfectly randomly disordered alloy, thus we expect that the topological nodal-line phase could be observed even upon a high level of alloying [80–84], as in the case of $\text{Zr}_5\text{Pt}_3\text{C}_{0.5}$.

5. Conclusions

In summary, we presented the superconducting properties of the interstitial carbon-doped compound $\text{Zr}_5\text{Pt}_3\text{C}_{0.5}$ by using magnetization, resistivity, specific heat and muon spin rotation and relaxation measurements. Magnetization data corroborates the bulk superconductivity at $T_C = 3.8$ K. The depolarization rate of the muon spin (σ_{sc}) in the FC mode is almost constant at low temperatures and it can be well modeled considering a fully gapped isotropic s -wave superconducting order parameter, with $2\Delta/k_B T_C = 3.84$, somewhat higher than 3.53, the value expected for BCS superconductors. The London penetration depth, superconducting carrier density and its effective mass are also estimated from the TF- μ SR analysis. Furthermore, the zero field μ SR confirms that there is no spontaneous magnetic moment, thus demonstrating that TRS is preserved in the superconducting ground state. Additionally, we showed

through the DFT calculations that Zr_5Pt_3 is a topological Dirac nodal-line semimetal protected by 6_3 screw rotations and glide mirror planes of the $P6_3/mcm$ space group. Therefore, this work puts forward a large, unprecedented class of superconducting topological nodal-line semimetals to realize novel quantum states of matter.

Acknowledgments

PPF, RFJ, LEC, LTFE and AJSM gratefully acknowledge the financial support of the São Paulo Research Foundation (FAPESP) under Grants 2013/07296-2, 2018/08819-2, 2019/05005-7, 2019/14359-7, 2019/26141-6 and 2020/08258-0. KP acknowledge the financial support from DST India for Inspire Fellowship (IF170620). AB would like to acknowledge DST India for Inspire Faculty Research Grant (DST/INSPIRE/04/2015/000169), the SERB, India, for core research grant support, and UK-India Newton funding for funding support. DTA would like to thank the Royal Society of London for Newton Advanced Fellowship funding and International Exchange funding between UK and Japan. The research was carried out using high-performance computing resources made available by the Superintendência de Tecnologia da Informação (STI), Universidade de São Paulo. The authors also acknowledge the National Laboratory for Scientific Computing (LNCC/MCTI, Brazil) for providing HPC resources of the SDumont supercomputer, which have contributed to the research results reported within this paper. This study was also financed by the Coordenação de Aperfeiçoamento de Pessoal de Nível Superior—Brasil (CAPES)—Finance Code 001, and CNPq, Grant No. 301463/2019-0.

Data availability statement

The data that support the findings of this study will be openly available following an embargo at the following URL/DOI: <https://doi.org/10.5286/ISIS.E.RB1920167-1>. Data will be available from 04 May 2024.

ORCID iDs

A Bhattacharyya  <https://orcid.org/0000-0002-8037-0487>
 P P Ferreira  <https://orcid.org/0000-0002-1135-0570>
 K Panda  <https://orcid.org/0000-0003-4305-9566>
 L R de Faria  <https://orcid.org/0000-0001-6044-5106>
 D T Adroja  <https://orcid.org/0000-0003-2280-079X>
 K Yokoyama  <https://orcid.org/0000-0001-6136-1908>

References

- [1] Haldane F D M 2004 *Phys. Rev. Lett.* **93** 206602
- [2] Xu G, Weng H, Wang Z, Dai X and Fang Z 2011 *Phys. Rev. Lett.* **107** 186806
- [3] Weng H, Yu R, Hu X, Dai X and Fang Z 2015 *Adv. Phys.* **64** 227–82
- [4] Shekhar C *et al* 2015 *Nat. Phys.* **11** 645–9
- [5] Liang T, Gibson Q, Ali M N, Liu M, Cava R J and Ong N P 2015 *Nat. Mater.* **14** 280–4
- [6] Zhao Y *et al* 2015 *Phys. Rev. X* **5** 031037
- [7] Li H, He H, Lu H Z, Zhang H, Liu H, Ma R, Fan Z, Shen S Q and Wang J 2016 *Nat. Commun.* **7** 1–7
- [8] Gao W *et al* 2017 *Phys. Rev. Lett.* **118** 256601
- [9] Zyuzin A A and Burkov A A 2012 *Phys. Rev. B* **86** 115133
- [10] Parameswaran S, Grover T, Abanin D, Pesin D and Vishwanath A 2014 *Phys. Rev. X* **4** 031035
- [11] Xiong J, Kushwaha S K, Liang T, Krizan J W, Hirschberger M, Wang W, Cava R J and Ong N P 2015 *Science* **350** 413–6
- [12] Huang X *et al* 2015 *Phys. Rev. X* **5** 031023
- [13] Hsieh D, Qian D, Wray L, Xia Y, Hor Y S, Cava R J and Hasan M Z 2008 *Nature* **452** 970–4
- [14] Hsieh D *et al* 2009 *Science* **323** 919–22
- [15] Zhang H, Liu C-X, Qi X-L, Dai X, Fang Z and Zhang S-C 2009 *Nat. Phys.* **5** 438–42
- [16] Beenakker C W J 2013 *Annu. Rev. Condens. Matter Phys.* **4** 113–36
- [17] Sürgers C, Gajdzik M, Fischer G, Löhneysen H v, Welter E and Attenkofer K 2003 *Phys. Rev. B* **68** 174423
- [18] Lv B, Zhu X Y, Lorenz B, Wei F Y, Xue Y Y, Yin Z P, Kotliar G and Chu C W 2013 *Phys. Rev. B* **88** 134520
- [19] Xu Y, Jöhr S, Das L, Kitagawa J, Medarde M, Shiroka T, Chang J and Shang T 2020 *Phys. Rev. B* **101** 134513
- [20] Zhang Y, Wang B, Xiao Z, Lu Y, Kamiya T, Uwatoko Y, Kageyama H and Hosono H 2017 *npj Quantum Mater.* **2** 1–7
- [21] Zheng C, Mattausch H and Simon A 2002 *J. Alloys Compd.* **347** 79–85
- [22] Cort B, Giorgi A L and Stewart G R 1982 *J. Low Temp. Phys.* **47** 179–85
- [23] Bortolozzo A D, Dos Santos C A M, Jardim R F, Ritter C, Devishvili A, Rotter M, Gandra F G and Machado A J S 2012 *J. Appl. Phys.* **111** 123912
- [24] Hamamoto S and Kitagawa J 2018 *Mater. Res. Express* **5** 106001
- [25] Renosto S, Lang R, Manesco A, Rodrigues D Jr, Santos F, Machado A, Baldan M and Diez E 2018 arXiv:1809.05008
- [26] Claesson T, Ivarsson J and Rasmussen S E 1977 *J. Appl. Phys.* **48** 3998–9
- [27] Bernevig A, Weng H, Fang Z and Dai X 2018 *J. Phys. Soc. Japan* **87** 041001
- [28] Weng H, Liang Y, Xu Q, Yu R, Fang Z, Dai X and Kawazoe Y 2015 *Phys. Rev. B* **92** 045108
- [29] Yu R, Weng H, Fang Z, Dai X and Hu X 2015 *Phys. Rev. Lett.* **115** 036807
- [30] Chan Y-H, Chiu C-K, Chou M Y and Schnyder A P 2016 *Phys. Rev. B* **93** 205132
- [31] Lee S L, Cywinski R and Kilcoyne S 1999 *Muon Science: Muons in Physics, Chemistry and Materials* vol 51 (Boca Raton, FL: CRC Press)
- [32] Bhattacharyya A 2020 Investigation of strong electronic interaction and signature of nodal superconductivity in $Zr_5Pt_3Co_{0.3}$: μ SR study *STFC ISIS Neutron and Muon Source* <https://data.isis.stfc.ac.uk/doi/study/108675792>
- [33] Pratt F L 2000 *Physica B* **289–290** 710–4
- [34] Kohn W and Sham L J 1965 *Phys. Rev.* **140** A1133
- [35] Hohenberg P and Kohn W 1964 *Phys. Rev.* **136** B864
- [36] Dal Corso A 2014 *Comput. Mater. Sci.* **95** 337–50
- [37] Giannozzi P *et al* 2009 *J. Phys.: Condens. Matter* **21** 395502
- [38] Giannozzi P *et al* 2017 *J. Phys.: Condens. Matter* **29** 465901
- [39] Perdew J P and Zunger A 1981 *Phys. Rev. B* **23** 5048
- [40] Monkhorst H J and Pack J D 1976 *Phys. Rev. B* **13** 5188
- [41] Marzari N, Vanderbilt D, De Vita A and Payne M C 1999 *Phys. Rev. Lett.* **82** 3296
- [42] Prozorov R and Kogan V G 2018 *Phys. Rev. Appl.* **10** 014030
- [43] Tinkham M 1975 *Introduction to Superconductivity* (Malabar, FL: Krieger)
- [44] Brandt E H 2008 *Physica B* **404** 695–9

- [45] Bhattacharyya A, Adroja D T, Smidman M and Anand V 2018 *Sci. China: Phys., Mech. Astron.* **61** 1–22
- [46] Adroja D *et al* 2017 *Phys. Rev. B* **96** 144502
- [47] Bhattacharyya A *et al* 2019 *Phys. Rev. Lett.* **122** 147001
- [48] Brandt E H 1988 *J. Low Temp. Phys.* **73** 355–90
- [49] Brandt E H 2003 *Phys. Rev. B* **68** 054506
- [50] Prozorov R and Giannetta R W 2006 *Supercond. Sci. Technol.* **19** R41
- [51] Adroja D T *et al* 2015 *Phys. Rev. B* **92** 134505
- [52] Adroja D *et al* 2017 *J. Phys. Soc. Japan* **86** 044710
- [53] Bhattacharyya A, Panda K, Adroja D T, Kase N, Biswas P K, Saha S, Das T, Lees M R and Hillier A D 2020 *J. Phys.: Condens. Matter* **32** 085601
- [54] Adroja D T *et al* 2021 *Phys. Rev. B* **103** 104514
- [55] Sonier J E, Brewer J H and Kieff R F 2000 *Rev. Mod. Phys.* **72** 769
- [56] Chia E E M, Salamon M B, Sugawara H and Sato H 2004 *Phys. Rev. B* **69** 180509
- [57] Amato A 1997 *Rev. Mod. Phys.* **69** 1119
- [58] McMillan W L 1968 *Phys. Rev.* **167** 331
- [59] Bhattacharyya A, Adroja D T, Quintanilla J, Hillier A, Kase N, Strydom A and Akimitsu J 2015 *Phys. Rev. B* **91** 060503
- [60] Bhattacharyya A, Adroja D T, Kase N, Hillier A, Akimitsu J and Strydom A 2015 *Sci. Rep.* **5** 1–8
- [61] Bhattacharyya A, Adroja D T, Kase N, Hillier A, Strydom A and Akimitsu J 2018 *Phys. Rev. B* **98** 024511
- [62] Panda K, Bhattacharyya A, Adroja D T, Kase N, Biswas P K, Saha S, Das T, Lees M R and Hillier A D 2019 *Phys. Rev. B* **99** 174513
- [63] Floris A, Sanna A, Massidda S and Gross E 2007 *Phys. Rev. B* **75** 054508
- [64] Bersier C, Floris A, Sanna A, Profeta G, Continenza A, Gross E K U and Massidda S 2009 *Phys. Rev. B* **79** 104503
- [65] Flores-Livas J A and Sanna A 2015 *Phys. Rev. B* **91** 054508
- [66] Kawamura M, Akashi R and Tsuneyuki S 2017 *Phys. Rev. B* **95** 054506
- [67] Ferreira P, Santos F, Machado A, Petrilli H and Eleno L 2018 *Phys. Rev. B* **98** 045126
- [68] Pascut G L, Widom M, Haule K and Quader K F 2019 *Phys. Rev. B* **100** 125114
- [69] Bhattacharyya A, Ferreira P, Santos F, Adroja D T, Lord J, Correa L, Machado A, Manesco A and Eleno L T 2020 *Phys. Rev. Res.* **2** 022001
- [70] Zhao Y, Lian C, Zeng S, Dai Z, Meng S and Ni J 2020 *Phys. Rev. B* **101** 104507
- [71] Correa L E, Ferreira P P, de Faria L R, Dorini T T, Fisk Z, Torikachvili M S, Eleno L T and Machado A J 2021 arXiv:2102.04812
- [72] Burkov A A, Hook M D and Balents L 2011 *Phys. Rev. B* **84** 235126
- [73] Fang C, Chen Y, Kee H Y and Fu L 2015 *Phys. Rev. B* **92** 081201
- [74] Fang C, Weng H, Dai X and Fang Z 2016 *Chin. Phys. B* **25** 117106
- [75] Yu R, Fang Z, Dai X and Weng H 2017 *Front. Phys.* **12** 1–14
- [76] Young S M, Zaheer S, Teo J C Y, Kane C L, Mele E J and Rappe A M 2012 *Phys. Rev. Lett.* **108** 140405
- [77] Yang B J and Nagaosa N 2014 *Nat. Commun.* **5** 1–10
- [78] Yang B-J, Morimoto T and Furusaki A 2015 *Phys. Rev. B* **92** 165120
- [79] Ferreira P P, Manesco A L R, Dorini T T, Correa L E, Weber G, Machado A J S and Eleno L T F 2021 *Phys. Rev. B* **103** 125134
- [80] Dziawa P *et al* 2012 *Nat. Mater.* **11** 1023–7
- [81] Narayan A, Di Sante D, Picozzi S and Sanvito S 2014 *Phys. Rev. Lett.* **113** 256403
- [82] Yan C *et al* 2014 *Phys. Rev. Lett.* **112** 186801
- [83] Lu H, Zhang X, Bian Y and Jia S 2017 *Sci. Rep.* **7** 1–10
- [84] Thirupathiah S *et al* 2018 *Phys. Rev. B* **98** 085145